Available online at www.sciencedirect.com

SCIENCE DIRECT®

Journal of Electron Spectroscopy and Related Phenomena 152 (2006) 67–77

JOURNAL OF ELECTRON SPECTROSCOPY and Related Phenomena

www.elsevier.com/locate/elspec

Theoretical investigation of the energy resolution of an ideal hemispherical deflector analyzer and its dependence on the distance from the focal plane

T.J.M. Zouros [a,b,*]

[a] Deptartment of Physics, University of Crete, P.O. Box 2208, 71003 Heraklion, Crete, Greece
[b] Institute of Electronic Structure and Laser, P.O. Box 1527, 71110 Heraklion, Crete, Greece

Received 19 May 2005; received in revised form 13 March 2006; accepted 15 March 2006
Available online 30 March 2006

Abstract

In most modern hemispherical deflector analyzers (HDAs) using a position sensitive detector (PSD), due to practical geometrical constraints (fringing field correctors, grids etc.), the PSD cannot always be placed at the optimal position, i.e. the first-order focal plane following 180° deflection at $h = 0$. Here, the dependence of the exit radial base width $\Delta r^*_{\pi h}$, base energy resolution $\mathcal{R}_{Bh}$ and line shape L_h on the distance h between the focal plane and the detection plane for an *ideal* HDA (no fringing fields) is investigated theoretically as a function of the maximum injection angle α^*_{max} and the diameter of the entry aperture Δr_0. Both exact numerical results and practical analytic formulas based on Taylor series expansions developed for any HDA show $\mathcal{R}_{Bh}$ and L_h become increasingly degraded with increasing h from their optimal values at $h = 0$. A detailed comparison of the resolution properties of conventional and biased paracentric HDAs is also presented. Apart from a few marginal improvements of limited utility, overall, the *ideal* paracentric HDA does not seem to have any distinct practical advantages over the conventional HDA. Resolution improvements recently reported for non-ideal paracentric HDAs must therefore be due to their strong fringing fields and needs to be further investigated. Our ideal HDA results provide a unique standard to evaluate the resolution performance of any HDA under realistic non-zero h-value conditions.

PACS: 07.81.+a

Keywords: Electron spectroscopy; ESCA; Hemispherical analyzer; Paracentric hemispherical analyzer; Fringing fields; Position sensitive detection

1. Introduction

High resolution electron spectroscopy (as for example electron spectroscopy for chemical analysis (ESCA) [1–3] or Auger electron spectroscopy (AES) [4]) is a mature technique utilized in many different fields of physics, material science, chemistry and even biology and medicine. One of the most popular spectrometers in use today is the hemispherical deflector analyzer (HDA) also available commercially from many different high tech companies. Today's, modern high power HDAs are equipped with state-of-the art multi-element zoom lens and position sensitive detector (PSD) [5–9] and therefore enjoy a very large collection efficiency.

In the past, when high resolution HDAs had a much lower throughput (no PSD) emphasis was primarily given to the optimization of the resolution [10] for highest étendue (the product of entrance area and solid angle) [11,12] or highest transmitted current [13,14]. The line shape was also investigated theoretically [12,15–19] using both analytic piecewise integration [12,18–20] and Monte Carlo techniques [15,21,16,22]. However, today, with the existing high throughput of modern ESCA spectrometers, high resolution has become of utmost importance. For an ideal HDA, the resolution is primarily determined by the maximum injection angle α^*_{max} and the diameter of the entry aperture or slit (real or virtual) Δr_0. First-order focusing is known to take place after deflection through 180° within the HDA and therefore the PSD should in principle be placed at this focal plane. However, in practice, due to geometrical constraints imposed primarily by field corrector schemes (grids, fringing field corrector rings, Jost apertures, see Ref. [23] for a recent

* Tel.: +30 2810 394117; fax: +30 2810 394101.
E-mail address: tzouros@physics.uoc.gr (T.J.M. Zouros).

0368-2048/$ – see front matter © 2006 Elsevier B.V. All rights reserved.
doi:10.1016/j.elspec.2006.03.007

update) the PSD must be placed at a small distance h ∼5–20 mm from the ideal HDA focal plane at $h = 0$. While the HDA resolution formula at $h = 0$ is well known and discussed in practically all reviews dealing with electron spectroscopy (see for example Refs. [18,19,24,25]), to our knowledge, there have been no investigations of the HDA energy resolution for $h > 0$. Thus, there is no way to extrapolate the energy resolution from $h = 0$ to realistic positive h-values, to quantify its expected deterioration and to know its dependence on $\alpha^*_{\max}$ and Δr_0. The only h-dependence study known to us, reports on a related subject also of importance to PSD usage, i.e. the possible reduction of energy non-linearity in the exit radial position along a PSD for $h > 0$ [26].

Of special interest in this presentation is the investigation of the so called *biased paracentric* HDA [27–29], i.e. an HDA whose entry radius R_0 is not at the traditional mean radius $\bar{R}$ and whose value of the entry potential $V_0 \equiv V(R_0)$ is biased (non-zero) rather than zero, as in most conventional HDAs. Such an HDA was recently shown in simulation [27] to have an improved energy resolution over that of an equal size conventional HDA and has been used with good results in the author's laboratory for high resolution Auger projectile electron spectroscopy of ion–atom collisions [30]. The simulation [27] investigated the case of a realistic HDA with large interradial spacing between inner and outer electrode and thus included the effect of the strong fringing fields at both the entry and the exit of the HDA thought to be responsible for the resolution improvement. While the reason for this improvement is still under investigation [31,32], it is of interest to also study the energy resolution of such an HDA in the absence of strong fringing fields, i.e. for ideal fields, and compare to that of the conventional HDA.

Here, we explore theoretically the energy resolution of an *ideal* HDA for $h \geq 0$ and its dependence on $\alpha^*_{\max}$ and Δr_0. We utilize both exact numerical and approximate analytic techniques to investigate the h-dependence of the exit radial base width $\Delta r^*_{\pi h}$, the base energy resolution $\mathcal{R}_{\mathrm{B}h}$ and the response function or line shape L_h of a generalized *ideal* HDA, thus including both conventional and paracentric [27–29] HDAs in one unified treatment.

2. Ideal hemispherical deflector analyzer

2.1. Generalized HDA—basic definitions

The most general type of HDA utilizes an *elliptical central tuning* trajectory [28]. Such a trajectory enters the HDA with an incidence angle $\alpha^* = 0$, radial position R_0 and nominal kinetic energy w (in this case also the *tuning energy*) and exits at radial position R_π after a deflection through 180° inside the HDA. All other rays enter the HDA at radial position r_0, incidence angle α^* and nominal pass energy t, exiting after deflection through 180° at radial position r^*_π and exiting angle α^*_π. We also introduce the fractional pass energy:

$$\tau \equiv \frac{t}{w} \tag{1}$$

so that the central tuning trajectory will always have $\tau = 1$. Finally, we define the *paracentricity* parameter ξ:

$$\xi \equiv \frac{\bar{R}}{R_0} \tag{2}$$

where $\bar{R} = (R_1 + R_2)/2$ is the mean HDA radius. In the past [28] we have always dealt with HDAs for which $R_\pi = \bar{R}$ (convenient but not necessary) for which $\xi = R_\pi/R_0$, in this case. We shall continue assuming $R_\pi = \bar{R}$, also here, but will maintain both symbols for generality.

We next introduce the concept of HDA entry bias. This refers to the value of the potential $\tilde{V}_0 \equiv \tilde{V}(R_0)$ at the central tuning ray entry radius R_0. Thus, we define the *biasing* parameter γ so that [28]:

$$q\tilde{V}_0 \equiv q\tilde{V}(R_0) = (1 - \gamma)w \tag{3}$$

where q is the particle charge (for electrons $q = -|e|$ with $e = 1.61 \times 10^{-19}$ C) and $\tilde{V}(r)$ is the potential inside the HDA [33], in this paper assumed to be *ideal* and given by:

$$\tilde{V}(r) = -\frac{k}{r} + c \tag{4}$$

Then, for $\gamma = 1$, $\tilde{V}_0 = 0$ the HDA is *unbiased*, while in general for $\gamma \neq 1$ the HDA is *biased*. The combination of ξ and γ define the particular type of HDA. Thus, conventional HDAs have $\tilde{V}_0 = 0$ and $R_0 = R_\pi = \bar{R}$. They are therefore unbiased with $\gamma = \xi = 1$ and their central tuning trajectory is a *circle*. Biased paracentric HDAs with ξ both larger and smaller than 1 have been reported. These, in general, will have an elliptic central tuning trajectory. Thus, for example, Belov et al. [34] describe an HDA with $R_0 > \bar{R}$ ($\xi < 1$) without, however, giving specifics about the actual values of ξ and γ used. Benis et al., used an HDA with $\xi = 1.2308$ and $\gamma = 1.5$ [30] for which SIMION electron optic simulations showed improved focusing over equal size conventional HDA [27,28]. In Table 1 we summarize typical values of HDA parameters.

2.2. h-Dependence of the exit radius $r^*_{\pi h}$

In Ref. [28] it was shown that a particle moving in the ideal $1/r$ potential $\tilde{V}(r)$ (see Eq. (4)) of an HDA tuned to the central tuning ray's nominal pass energy w, entering at radius r_0 with energy τ and incidence angle α^*, after a deflection through 180° inside the HDA (see Fig. 1) will exit at the radius r^*_π given by:

$$r^*_\pi \equiv r^*_\pi(r_0, \alpha^\star, \tau) = -r_0 + \frac{D_0}{1 + \kappa(1 - \tau\cos^2\alpha^\star)} \tag{5}$$

with

$$D_0 \equiv R_0 + R_\pi = (1 + \xi)R_0 \geq 2R_0 \tag{6}$$

$$\kappa \equiv \frac{\xi}{\gamma} \tag{7}$$

and potential constants k and c given by:

$$qk = \frac{wD_0}{\kappa} \tag{8}$$

$$qc = w\left(1 + \frac{1}{\kappa}\right) \tag{9}$$

Table 1
Comparison of equal size paracentric and conventional HDA parameters [28] for electrons ($q = -e$)

Parameter	Value	Description
R_1 (mm)	72.4	HDA inner radius
R_2 (mm)	130.8	HDA outer radius
$\bar{R}$ (mm)	101.6	HDA mean radius $\bar{R} \equiv (R_1 + R_2)/2$
R_π (mm)	101.6	Central ray exit radius $r_\pi = R_\pi$
Δr_d (mm)	~ 0.2	PSD position resolution
d_0 (mm)	6	HDA entry diameter
$d_{\rm PSD}$ (mm)	40	PSD active diameter
w	W/F	Nominal central ray pass energy (HDA tuning energy)
F	W/w	Retardation factor
τ	t/w	Fractional pass energy

Parameter	Description
t	Pass energy after retardation $t = T + V_{\rm p}$, $V_{\rm p} < 0$
$V_{\rm p}$	HDA retarding plate voltage $V_{\rm p} = w - W < 0$
T	Energy prior to retardation
W	Central ray energy prior to retardation $W > w$
r_0	HDA entry radius
α^*, (α)	Angle of incidence at HDA entry prior, (after) refraction
r^*_π, $(r^*_{\pi h})$	HDA exit radius at $h = 0$, $(h > 0)$ *corrected* for refraction
r_π, $(r_{\pi h})$	HDA exit radius at $h = 0$, $(h > 0)$ *uncorrected* for refraction
α_π (α^*_π)	Angle of incidence at HDA exit prior, (after) refraction

Parameter	Paracentric HDA	Conventional HDA	Paracentric HDA	
R_0 (mm)	82.5	101.6	120.65	Central ray entry radius
D_0 (mm)	184.15	203.2	222.25	Central ray range $D_0 \equiv R_0 + R_\pi$
$\tilde{V}_0$	$0.5w$	0	$-0.6w$	HDA entry bias $\tilde{V}_0 \equiv \tilde{V}(R_0) = (\gamma - 1)w$
γ	1.5	1	0.4	Biasing parameter
ξ	1.2308	1	0.842105	Paracentricity $\xi \equiv \bar{R}/R_0$
κ	0.82053	1	2.10526	$\kappa \equiv \xi/\gamma$
$\bar{D}$ (mm)	151.1	203.2	467.895	Mean dispersion $\bar{D} = D_0\kappa$

For definitions also refer to Fig. 1 and Eqs. (5)–(9)

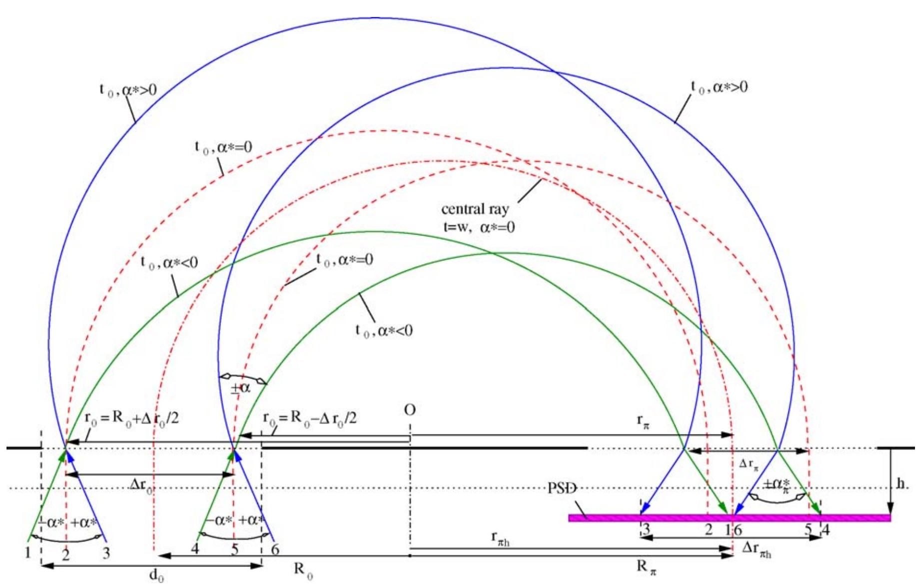

Fig. 1. Schematic electron trajectories in a typical HDA spectrometer. The drawing is not to scale. The PSD is placed a distance h from the focusing plane of the HDA. Two sets of trajectories with the same energy t_0 and positive, negative and zero injection angle α^* are shown. Their starting points are at the two limits of the (virtual) entry aperture having diameter Δr_0 centered at $r = R_0$. d_0 is the diameter of the actual *physical* entry aperture. Trajectory 3 with $\alpha^* = \alpha^*_{\rm max}$ always leads to the minimum exit radius, $r^*_{\pi h\,\rm min}$ (Eq. (18)). Trajectory 4 with $\alpha^* = \alpha^*_{m0}$ (Eq. (20)) always leads to the maximum exit radius $r^*_{\pi h\,\rm max}$ (Eq. (25)). The difference between the maximum and minimum radii is the base exit radial width $\Delta r^*_{\pi h}$ (Eq. (26)) which together with the dispersion length D determines the base energy resolution (Eq. (37)).

Table 2
Comparison of central ray ($r_0 = R_0, \alpha^* = 0$) exit radii r^*_π (evaluated using Eq. (5)) along the focal plane ($h = 0$) for biasing parameter $\gamma = 1$ and 1.5 and nominal fractional pass energy $\tau_0 = 0.9, 1, 1.1$

γ	τ_0	r^*_π(mm)	
		Paracentric HDA	Conventional HDA
1	0.9	81.419	83.127
1.5	0.9	87.636	88.900
1	1	101.600	101.600
1.5	1	101.600	101.600
1	1.1	127.446	124.178
1.5	1.1	118.060	116.114

For the paracentric HDA we use $\xi = 1.2308$ and $R_0 = 82.55$ mm, while for the conventional HDA we use $\xi = 1$ and $R_0 = R_\pi = 101.6$ mm.

Table 2 lists values of r^*_π for different values of γ and ξ.

For an *ideal* HDA tuned to the nominal pass energy w [24], the voltages are set once γ has been specified. They are given by Ref. [28]:

$$qV_i \equiv qV(R_i) = q\tilde{V}_i + qV_{\rm p} \tag{10}$$

$$qV_i = w\left[F - \left(\frac{\gamma}{\xi}\right)\left(\frac{D_0}{R_i} - 1\right)\right] \tag{11}$$

for $i = 1, 2$ and $qV_{\rm p} = W - w$, the plate voltage used with preretardation. F is the retardation factor, given by $F = W/w$, where W is the original undecelerated "tuning energy" of the HDA [28] (source central ray kinetic energy). Thus, in cases where no pre-retardation is used prior to energy analysis, $V_{\rm p} = 0$ and $F = 1$.

In a *conventional* HDA, with electrode voltages V_i given by Eq. (11), $\tilde{V}_0 = 0$ (i.e. $\gamma = 1$), so that it is matched to the potential outside the HDA also assumed to be zero. Thus, particles entering the HDA at $r_0 = R_0$ will not be refracted at the HDA potential boundary and the angle of incidence α^* equals the angle of refraction α, i.e. $\alpha^* = \alpha$. However, at any other radius $r_0 \neq R_0$ or for a *biased* HDA (i.e. $\gamma \neq 1$ see Eq. (3)), differences in potentials on either side of the potential boundary will result in refraction so that in general $\alpha^* \neq \alpha$ [28]. In deriving Eq. (5) in Ref. [28] it was assumed that the potential changes in a sharp step-like manner in crossing the boundary. In a real HDA this potential step is, of course, more gradual.

The effect of refraction has been included in the above formula for r^*_π (Eq. (5)) as discussed in detail in Ref. [28]. On exiting the HDA, the charged particle is again refracted at the potential boundary exiting with angle α^*_π. It then travels through the drift region, impinging on the PSD plane (at a distance h) at the axial distance $r^*_{\pi h}$, as shown in Fig. 1, given by:

$$r^*_{\pi h} = r^*_\pi + h\,\tan\,\alpha^*_\pi \tag{12}$$

Paying close attention to the sign of α^* [15] conventionally defined such that $\alpha^* > 0$ when the electron's radial distance r increases at entry (see Figs. 2–4 in Ref. [28]) and using the relation between α^*_π and α^* (see Eq. (32) in Ref. [28]) we have:

$$\tan\,\alpha^*_\pi = -\frac{r^*_\pi}{r_0}\,\tan\,\alpha^* \tag{13}$$

we can then write:

$$r^*_{\pi h} = r^*_{\pi h}(r_0, \alpha^*, \tau, h) = r^*_\pi\left(1 - \frac{h}{r_0}\,\tan\,\alpha^*\right) \tag{14}$$

which gives the radial distance from the axis of symmetry for a particle hitting a PSD placed a distance h from the HDA exit plane. From Eq. (14) it is clear that for the same entry point r_0, positive injection angles ($\alpha^* > 0$) always lead to smaller values of $r^*_{\pi h}$ than negative injection angles ($\alpha^* < 0$).

We also define the dispersion length $D \equiv D(\tau_0)$ for an *ideal* HDA utilizing a PSD as:

$$D \equiv \tau_0 \frac{\partial r^*_{\pi h}}{\partial \tau}\bigg|_{r_0=R_0,\alpha^*=0,\tau=\tau_0} = \tau_0 \frac{\bar{D}}{X(\tau_0)^2} = \tau_0 \frac{D_0 \kappa}{X(\tau_0)^2} \tag{15}$$

where $X \equiv X(\tau_0) = 1 + \kappa(1 - \tau_0)$.

Our definition of the dispersion length D is seen to be dependent on the particle's fractional pass energy, τ_0, thus allowing for the inclusion of HDAs with PSD, having a large acceptance energy window around the central ray energy $\tau_0 = 1$. Then, the mean dispersion length $\bar{D} \equiv D(\tau_0 = 1) = D_0\kappa$ corresponds to the traditional dispersion length used with slit spectrometers. For $\kappa = 1$ (conventional HDA) and $\tau_0 = 1$, we also have $X = 1$ and therefore $\bar{D} = D_0 = 2\bar{R}$. In Fig. 2 , the energy dependence of D is shown for a few different cases of interest for the HDAs listed in Table 1. As can be seen from Eq. (15), it is the ratio $\kappa = \xi/\gamma$ that determines the dispersion of the HDA. It is also seen that the highest dispersion HDAs have increasingly nonlinear energy dependence, of paramount importance for use with a PSD [26], particularly if the HDA voltages will be scanned for use at constant tuning energy w. Thus, while high dispersion

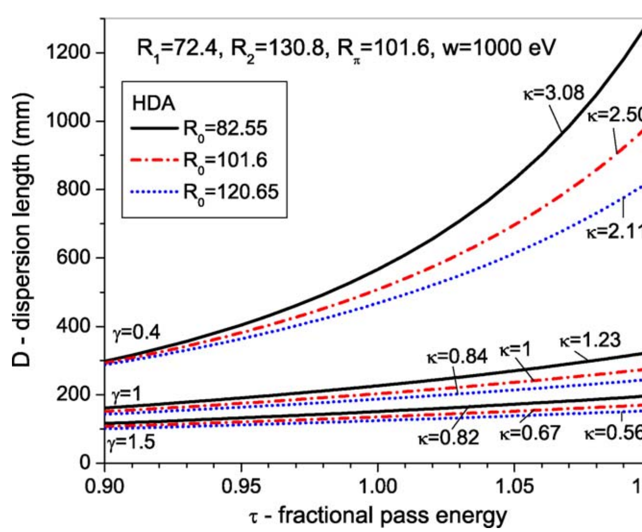

Fig. 2. Plot of the dispersion length D as a function of fractional pass energy τ (Eq. (15)) over a 20% energy window for an HDA with $R_1 = 72.4$ mm, $R_2 = 130.8$ mm and $\bar{R} = R_\pi = 101.6$, tuned to $w = 1000$ eV. Cases for three different entry radii are shown including $R_0 = 82.55, 101.6, 120.65$ mm corresponding to HDAs with paracentricity $\xi = \bar{R}/R_0 = 1.2308, 1, 0.8421$, respectively (see Table 1). Three different biases are also shown with $\gamma = 0.4, 1, 1.5$. D is seen to grow with increasing energy τ and $\kappa = \xi/\gamma$ (Eq. (7)). The linearity of D across the 20% PSD acceptance window shown is seen to be compromised with increasing κ.

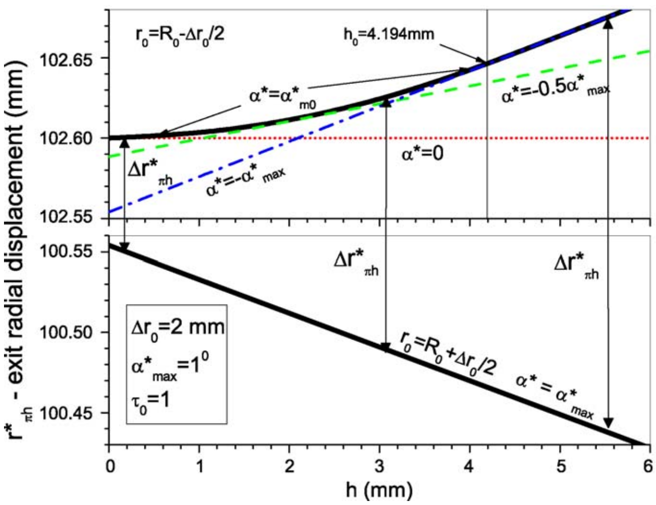

Fig. 3. Example of the h-Dependence of $r^*_{\pi h}(R_0 - \Delta r_0/2, \alpha^*, \tau_0, h)$ (top) and $r^*_{\pi h_{\min}} = r^*_{\pi h}(R_0 + \Delta r_0/2, \alpha^*_{\max}, \tau_0, h)$ (bottom) for the paracentric HDA having $\gamma = 1.5$, $\xi = 1.2308$ and $\alpha^*_{\max} = 1°$. The continuous (black) lines mark the locus of $r^*_{\pi h\,\max}$ (top) (with $\alpha^* = \alpha^*_{m0}$—Eq. (25)) and $r^*_{\pi h\,\min}$ (bottom) (Eq. (18)). The other three lines (top) mark examples of electron trajectories having $\alpha^* = 0$ (dotted red line), $\alpha^* = -0.5\alpha^*_{\max}$ (dashed green line) and $\alpha^* = -\alpha^*_{\max}$ (dashed-dot blue line), respectively. The position of h_0 given by Eq. (23) is marked. For $h \geq h_0$, $r^*_{\pi h}(R_0 - \Delta r_0/2, \alpha^*_{m0}, \tau_0, h)$ and $r^*_{\pi h}(R_0 - \Delta r_0/2, -\alpha^*_{\max}, \tau_0, h)$ merge. The angle α^*_{m0} is given by the solution of Eq. (20) and depends on h. An analytic approximation of α^*_{m0} is given in Eq. (29). The distance between the two thick black lines gives the exit radial base width $\Delta r^*_{\pi h} = r^*_{\pi h_{\max}} - r^*_{\pi h_{\min}}$, as indicated by the double headed arrows at three different values of h (for interpretation of the references to colour in this figure legend, the reader is referred to the web version of the article).

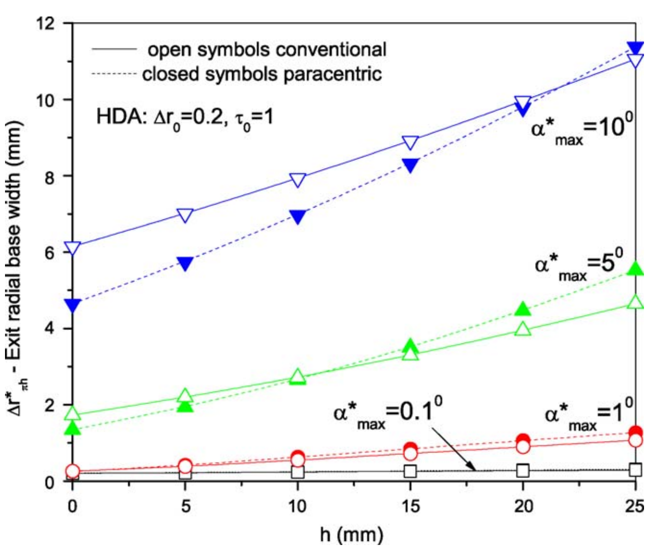

Fig. 4. h-Dependence of the exact exit radial base width $\Delta r^*_{\pi h}$. Open symbols refer to a conventional HDA ($\gamma = \xi = 1$), while closed symbols to the equal sized ($\bar{R} = 101.6$ mm) biased paracentric HDA ($\gamma = 1.5$, $\xi = 1.2308$). $\tau_0 = 1$ and $\Delta r_0 = 0.2$ mm. For large values of $\alpha^*_{\max}$ and small values of h, the paracentric HDA is seen to have a smaller radial base width $\Delta r^*_{\pi h}$ than the conventional HDA.

is always of interest, as it generally leads to the highest energy resolution, energy versus exit position non-linearities may limit the effectiveness of high dispersion, since the energy acceptance window of the PSD might need to be substantially reduced before acceptable linearity is recovered.

Recently, a biased paracentric HDA having $\xi = 1.2308$ and $\gamma = 1.5$, used by the author in zero-degree Auger projectile electron spectroscopy [30,35] was shown in electron optics simulations using SIMION [36,37] to have improved focusing properties over that of an equal size conventional HDA [27]. This property, not yet well understood, is most likely due to fringing field effects which are however, difficult to treat in general. Here, as a first step in trying to understand this result, we first consider just the *ideal* HDA and compare the focusing properties of the ideal paracentric HDA to those of the ideal conventional HDA. In the following, we use Eqs. (5) and (14) to investigate the exit radial base width $\Delta r^*_{\pi h}$, the base resolution $\mathcal{R}_{Bh}$ and the line shape L_h of an ideal HDA and their dependence on h.

2.3. h-Dependence of the HDA exit radial base width $\Delta r^*_{\pi h}$

The exit radial base width $\Delta r^*_{\pi h}$ is the maximum total length along the dispersion direction of the trace of the electron trajectory for a *monoenergetic* electron of fractional pass energy τ_0 due to the range of permissible input radii r_0 and injection angles $\alpha^\star$, i.e.

$$R_0 - \frac{\Delta r_0}{2} \leq r_0 \leq R_0 + \frac{\Delta r_0}{2} \tag{16}$$

$$-\alpha^*_{\max} \leq \alpha^* \leq \alpha^*_{\max} \tag{17}$$

$\alpha^*_{\max}$ and Δr_0 determine the line shape and base resolution of an ideal HDA. To reduce the tailing of the line shape due to the angular contributions, Kuyatt & Simpson [38] proposed that $D\alpha^{*2}_{\max} \leq \Delta r_0/2$, a condition strived for in most high resolution HDAs. Popular optimization conditions are discussed in detail and compared in Refs. [39,40]. For an HDA without a lens, Δr_0 is equal to the width of the real entry slit or aperture diameter d_0. However, for an HDA equipped with an injection lens, Δr_0 is the diameter of a *virtual* aperture given by the spot size of the lens focus. In the case of an injection lens, Δr_0 and $\alpha^*_{\max}$ are not anymore independent, but are related via the Helmholtz–Lagrange law. In this case, as we have recently shown for $h = 0$ [41], there is an optimal choice of Δr_0 and $\alpha^*_{\max}$ that leads to the best possible resolution of the HDA. Clearly, as long as $\Delta r_0 < d_0$, transmission is preserved. In Ref. [42] we use the results developed here to extend our optimization method [41] to the case of non-zero h. In this presentation, however, $\alpha^*_{\max}$ and Δr_0 will be assumed in all generality to be independent of one another.

2.3.1. Exact calculation

For $h > 0$ special care must be exercised in computing the exit radial base width, $\Delta r^*_{\pi h}$. In Fig. 1, pencils of angular divergence α^* are shown at either side of the entry aperture corresponding to the limiting cases. By inspection, we note that the minimum exit radial position $r^*_{\pi h\,\min}$ will always come from trajectory 3 having $\alpha^* = \alpha^*_{\max}$ and $r_0 = R_0 + \Delta r_0/2$ corresponding to:

$$r^*_{\pi h\,\min} = r^*_{\pi h}\left(R_0 + \frac{\Delta r_0}{2}, \alpha^*_{\max}, \tau_0, h\right) \tag{18}$$

Computing the maximum radius requires more attention. For $h = 0$, due to first order focusing and as shown in Fig. 1 trajectory 5 (having $\alpha^* = 0$) will always give the largest radius. Thus, we always have:

$$r^*_{\pi\max\pm} = r^*_{\pi}\left(R_0 \pm \frac{\Delta r_0}{2}, 0, \tau_0\right) = -R_0 \mp \frac{\Delta r_0}{2} + \frac{D_0}{X} \tag{19}$$

However, as seen from Fig. 1, for $h > 0$ trajectory 4 deriving from some negative injection angle α^*_{m0} not necessarily equal to $-\alpha^*_{\max}$ will mark the maximum radius $r^*_{\pi h\,\max}$. To find the angle α^*_{m0} at which $r^*_{\pi h}(R_0 - \Delta r_0/2, \alpha^*, \tau_0, h)$ is maximized the following conditions need to be fulfilled:

$$\frac{\partial}{\partial\alpha^*} r^*_{\pi h}\left(R_0 - \frac{\Delta r_0}{2}, \alpha^*, \tau_0, h\right)\bigg|_{\alpha^*_{m0}} = 0 \tag{20}$$

$$\frac{\partial^2}{\partial\alpha^{*2}} r^*_{\pi h}\left(R_0 - \frac{\Delta r_0}{2}, \alpha^*, \tau_0, h\right)\bigg|_{\alpha^*_{m0}} < 0 \tag{21}$$

Clearly, the solution, if it exists, $\alpha^*_{m0} = \alpha^*_{m0}(\tau_0, h)$ will depend on the value of h and τ_0. Then we shall always have:

$$r^*_{\pi h}\left(R_0 - \frac{\Delta r_0}{2}, \alpha^*_{m0}, \tau_0, h\right) \geq r^*_{\pi h}\left(R_0 - \frac{\Delta r_0}{2}, 0, \tau_0, h\right) \tag{22}$$

with the equality occurring at $h = 0$. In general $|\alpha^*_{m0}(\tau_0, h)|$ is found to increase monotonically with h, eventually reaching $\alpha^*_{\max}$ at some critical distance $h = h_0$. Since $\alpha^*_{\max}$ is the maximum allowed injection angle, any solutions $|\alpha^*_{m0}| > \alpha^*_{\max}$ are unphysical, and therefore for $h > h_0$, $|\alpha^*_{m0}|$ must be replaced by its limit $\alpha^*_{\max}$. Thus, h_0 must satisfy the equation,

$$|\alpha^*_{m0}(\tau_0, h_0)| = \alpha^*_{\max} \tag{23}$$

and in general will depend on Δr_0, $\alpha^*_{\max}$ and τ_0.

The complete solution for α^*_{m0} may thus be represented by the double branched function:

$$\alpha^*_{m0} = \begin{cases} \text{Solution of Eq.(20)} & \text{for } 0 \leq h \leq h_0 \\ -\alpha^*_{\max} & \text{for } h \geq h_0 \end{cases} \tag{24}$$

We may now evaluate $r^*_{\pi h}(R_0 - \Delta r_0/2, \alpha^*, \tau_0, h)$ at $\alpha^* = \alpha^*_{m0}$ using Eq. (24) to obtain $r^*_{\pi h\,\max}$. This necessarily leads to the double-branched function $r^*_{\pi h\,\max} \equiv r^*_{\pi h}(R_0 - \Delta r_0/2, \alpha^*_{m0}, \tau_0, h)$ given by:

$$r^*_{\pi h\,\max} = \begin{cases} r^*_{\pi h}\left(R_0 - \frac{\Delta r_0}{2}, \alpha^*_{m0}, \tau_0, h\right) & \text{for } 0 \leq h \leq h_0 \text{ (or } \leq |\alpha^*_{m0}| \leq \alpha^*_{\max}) \\ r^*_{\pi h}\left(R_0 - \frac{\Delta r_0}{2}, -\alpha^*_{\max}, \tau_0, h\right) & \text{for } h \geq h_0 \text{ (or } |\alpha^*_{m0}| \geq \alpha^*_{\max}) \end{cases} \tag{25}$$

The exit radial base width $\Delta r^*_{\pi h}$ is then defined as:

$$\Delta r^*_{\pi h} \equiv r^*_{\pi h\,\max} - r^*_{\pi h\,\min} \tag{26}$$

In Fig. 3 , we give an example for the paracentric HDA of $r^*_{\pi h}(R_0 - \Delta r_0/2, \alpha^*, \tau_0, h)$ (top) and $r^*_{\pi h}(R_0 + \Delta r_0/2, \alpha^*_{\max}, \tau_0, h)$ (bottom) and their dependence on h for the case of $\Delta r_0 = 2\,\text{mm}$, $\tau_0 = 1$ and $\alpha^*_{\max} = 1^\circ$. In the case of $r^*_{\pi h}(R_0 - \Delta r_0/2, \alpha^*, \tau_0, h)$, three different values of α^* including α^*_{m0} are shown. The exit radial base width $\Delta r^*_{\pi h}$ is also marked.

Evaluation of Eq. (26) can be performed *exactly*. It is only necessary to solve the transcendental equation Eq. (20) for α^*_{m0} numerically. Then, depending on whether $|\alpha^*_{m0}|$ is smaller or larger than $\alpha^*_{\max}$ the correct branch of Eq. (25) can be calculated. Therefore the value of h_0 is really superfluous to the calculation. However, since h is a physical distance, in principle directly measurable in the laboratory, while α^* is a much less accessible parameter, it is intuitively useful to also compute h_0.

In the sections to follow, we use the exact value of α^*_{m0} obtained by solving Eq. (20) numerically with Mathematica [43]. However, to obtain a better understanding of the various dependencies, analytic results are also presented using Taylor series expansions of the quantities of interest to first order in Δr_0 and to second order in $\alpha^*_{\max}$. These are also used in the resolution optimization presented in Ref. [42].

2.3.2. *Approximate analytic calculation*

A relatively simple analytic approximation to $r^*_{\pi h}$ can be obtained by using a Taylor series expansion of $r^*_{\pi h}(R_0 \pm \Delta r_0/2, \alpha^*, \tau_0, h)$ to first order in Δr_0 and to second order in $\alpha^*_{\max}$:

$$r^*_{\pi h}\left(R_0 \pm \frac{\Delta r_0}{2}, \alpha^*, \tau_0, h\right) \approx r^*_{\pi\max\pm} - h\alpha^*\left[G\left(1 \mp \frac{\Delta r_0}{2R_0}\right) - 1\right] - D\alpha^{*2} \tag{27}$$

with $r^*_{\pi\max\pm}$ given by Eq. (19) and where we have introduced the symbol:

$$G \equiv G(\tau_0) = D_0/(R_0 X) \tag{28}$$

with the mean value given by $\bar{G} = G(\tau_0 = 1) = D_0/R_0$. For a conventional HDA ($\kappa = \xi = 1$) we also have $G = 2/(2 - \tau_0)$ and $\bar{G} = 2$. Setting Eq. (27) into Eq. (20) and solving for α^*_{m0} we obtain the approximate analytic solution for α^*_{m0}. This can be represented as a double branched function in analogy to the exact solution Eq. (24):

$$\alpha^*_{m0} \approx \begin{cases} -\frac{h}{2D}\left[G\left(1 + \frac{\Delta r_0}{2R_0}\right) - 1\right] & \text{for } 0 \leq h \leq h_0 \\ -\alpha^*_{\max} & \text{for } h \geq h_0 \end{cases} \tag{29}$$

α^*_{m0} is indeed negative in value and also satisfies the condition for a maximum (Eq. (21)).

Using approximations Eqs. (27) and (29) to evaluate Eq. (26) we obtain the approximate analytic form of the base width $\Delta r^*_{\pi h}$:

$$\Delta r^*_{\pi h} \equiv \Delta r^*_{\pi h}(\Delta r_0, \alpha^*_{\max}, \tau_0, h) \approx \begin{cases} \Delta r_0 + h\alpha^*_{\max}\left[G\left(1-\frac{\Delta r_0}{2R_0}\right)-1\right] + D\alpha^{*2}_{\max} + \frac{h^2}{4D}\left[G\left(1+\frac{\Delta r_0}{2R_0}\right)-1\right]^2 & \text{for } 0 \le h \le h_0 \\ \Delta r_0 + 2h\alpha^*_{\max}(G-1) & \text{for } h \ge h_0 \end{cases} \quad (30)$$

with an approximate value for h_0 given by:

$$h_0 \equiv h_0(\Delta r_0, \alpha^*_{\max}, \tau_0) \approx \frac{2D\alpha^*_{\max}}{[G(1+(\Delta r_0/2R_0))-1]} \quad (31)$$

For $h = 0$ we obtain the well known formula for the base width Δr^*_π of an HDA at the focal plane:

$$\Delta r^*_\pi = \Delta r_0 + D\alpha^{*2}_{\max} \quad (32)$$

All the extra h-terms in $\Delta r^*_{\pi h}$ (Eq. (30)) can be shown to be positive and therefore the situation $h > 0$ always leads to larger base widths, i.e. $\Delta r^*_{\pi h} \ge \Delta r^*_\pi$. For $h = h_0$, both branches yield the same result namely:

$$\Delta r^*_{\pi h_0} = \Delta r_0 + \left[\frac{4(G-1)}{G(1+(\Delta r_0/2R_0))-1}\right] D\alpha^{*2}_{\max} \quad (33)$$

In Figs. 4 and 5, the exact values of $\Delta r^*_{\pi h}$ are plotted for equal size ($\bar{R} = 101.6$ mm) conventional ($R_0 = 101.6$, $\gamma = 1$) and biased paracentric ($R_0 = 82.55$, $\gamma = 1.5$) HDA with $\tau_0 = 1$ and entry angles $\alpha^*_{\max} = 0.1°, 1°, 5°, 10°$ at 6 different values of $h = 0, 5, 10, 15, 20, 25$ mm and for two different entry aperture diameters $\Delta r_0 = 2$ mm and $\Delta r_0 = 0.2$ mm. The general tendency is for $\Delta r^*_{\pi h}$ to increase with increasing h values. This tendency becomes stronger for increasing values of $\alpha^*_{\max}$. For $\alpha^*_{\max} = 0.1$–$1°$, $\Delta r^*_{\pi h}$ increases extremely slowly and is practically insensitive to changes in h. Interestingly, for small values of h the paracentric HDA exhibits smaller radial base widths than those of the conventional HDA.

2.4. h-Dependence of the HDA base resolution $\mathcal{R}_{Bh}$

For a beam of monoenergetic particles of pass energy t_0, the base resolution $\mathcal{R}_B$ of an energy analyzer tuned to the pass energy w is defined as the ratio of the transmitted (and detected) energy width Δt_B (the base width) over t_0:

$$\mathcal{R}_B \equiv \frac{\Delta t_B}{t_0} = \frac{\Delta \tau_B}{\tau_0} \quad (34)$$

$\mathcal{R}_B$ is a constant, dependent only on the geometrical parameters of the analyzer and independent of the pass energy t_0 (or equivalently τ_0). We can convert the maximum radial base width $\Delta r^*_{\pi h}$ computed in Eq. (30), to an energy width using the radial distance-to-energy conversion factor, which is seen from Eq. (15) to be just τ_0/D, where D is the HDA dispersion at τ_0. This is equivalent to the experimental energy versus position calibration of a PSD, typically performed in electron spectroscopy measurements. If we also include the width of the exit slit (or position resolution in case of a PSD) Δr_d, we get the total base energy width Δt_B (or equivalently $\Delta \tau_B$) [25] and therefore

$$\mathcal{R}_B = \frac{\Delta r^*_{\pi h} + \Delta r_d}{D}. \quad (35)$$

If we define S as the "slit" term given by the sum of the width of the slits (or virtual apertures) over the dispersion:

$$S \equiv S(\tau_0) = \frac{\Delta r_0 + \Delta r_d}{D} \quad (36)$$

then, using Eq. (26) or its approximation Eq. (30) and Eqs. (35) and (36), we finally obtain the base resolution $\mathcal{R}_{Bh} \equiv \mathcal{R}_{Bh}(\Delta r_0, \alpha^*_{\max}, \tau_0, h)$ given by:

$$\mathcal{R}_{Bh} = \begin{cases} S + \frac{h}{D}\alpha^*_{\max}\left[G\left(1-\frac{\Delta r_0}{2R_0}\right)-1\right] + \alpha^{*2}_{\max} + \frac{h^2}{4D^2}\left[G\left(1+\frac{\Delta r_0}{2R_0}\right)-1\right]^2 & \text{for } 0 \le h \le h_0 \\ S + \frac{2h}{D}\alpha^*_{\max}(G-1) & \text{for } h \ge h_0 \end{cases} \quad (37)$$

at $h = h_0$ both branches give the same result:

$$\mathcal{R}_{Bh_0} = S + \frac{4(G-1)\alpha^{*2}_{\max}}{G(1+(\Delta r_0/2R_0))-1} \quad (38)$$

For $h = 0$, we get from the first branch the well known result for the base resolution of an HDA along the focusing plane:

$$\mathcal{R}_B(\tau_0, h = 0) = S + \alpha^{*2}_{\max} = \frac{\Delta r_0 + \Delta r_d}{D} + \alpha^{*2}_{\max} \quad (39)$$

The base resolution is plotted as a function of h in Figs. 6 and 7. In general, a similar h-dependence is observed as for $\Delta r^*_{\pi h}$. However, now the base resolution for a paracentric

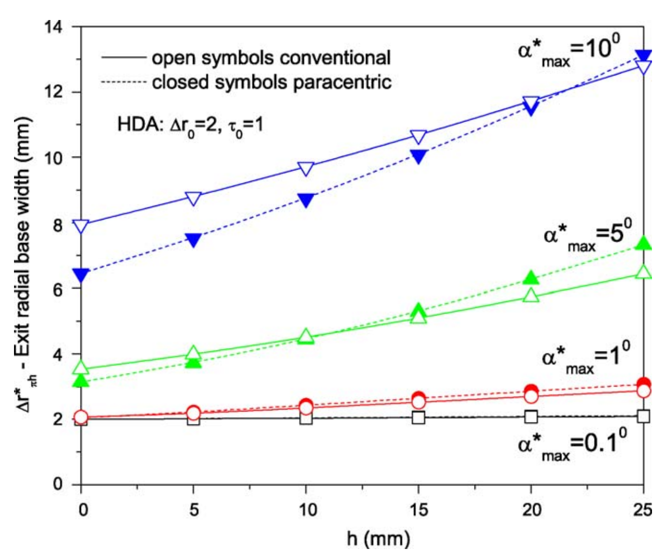

Fig. 5. Same as Fig. 4, but for $\Delta r_0 = 2$ mm.

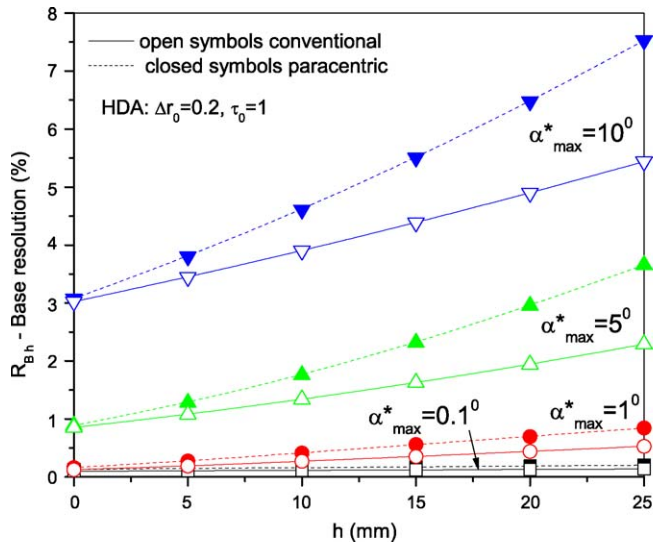

Fig. 6. Comparison of h-dependence of base resolution $\mathcal{R}_{Bh}$ for a conventional (open symbols) and paracentric (closed symbols) HDA of equal size ($\bar{R} = 101.6$ mm) for $\tau_0 = 1$ and $\Delta r_0 = 0.2$ mm.

($\gamma = 1.5$) HDA is shown to always be larger than that of the conventional ($\gamma = 1$) HDA. This has to do with the fact that the dispersion length D is largest for the smallest γ, as already discussed (see Eq. (15) and Fig. 2). Thus, a small $\Delta r^*_{\pi h}$ translates into a corresponding small $\mathcal{R}_{Bh}$ *only* for equal dispersion lengths.

2.5. h-Dependence of the HDA line shape L_h

As already pointed out, to limit the effect of the angular term and obtain a more symmetric line shape, Kuyatt and Simpson [38] proposed the following *criterion* for the ratio χ of the angular to the "slit" term:

$$\chi \equiv \frac{{\alpha^\star_{\max}}^2}{S} = \frac{D{\alpha^\star_{\max}}^2}{(\Delta r_0 + \Delta r_d)} \leq \frac{1}{2} \tag{40}$$

For non-zero h we can extend the Kuyatt-Simpson (KS) criterion to also incorporate the h-dependent terms. We therefore define a new ratio χ_h given by the ratio of the sum of both angular and h-dependent terms over the slit term:

$$\chi_h = \frac{R_{Bh}}{S} - 1 \tag{41}$$

which thus also becomes a double branched function. Directly from Eq. (40), it is clear that the smallest dispersion will always lead to the smallest χ_h. Therefore the biased paracentric HDA with $\gamma > 1$ will always have the smallest χ_h which will also be smallest at the lowest energy τ_0 and the smallest h. Thus, paracentric HDAs with $\gamma > 1$ can be expected, in principle, to provide an improved line shape. Whether this is also true for a real paracentric HDA with strong fringing fields is of course still an open question and will be explored in future publications [44,32].

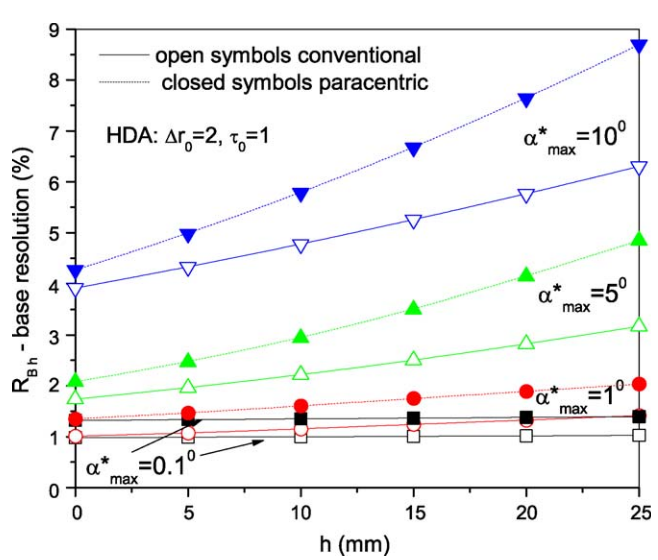

Fig. 7. Same as Fig. 6, but for $\Delta r_0 = 2$ mm.

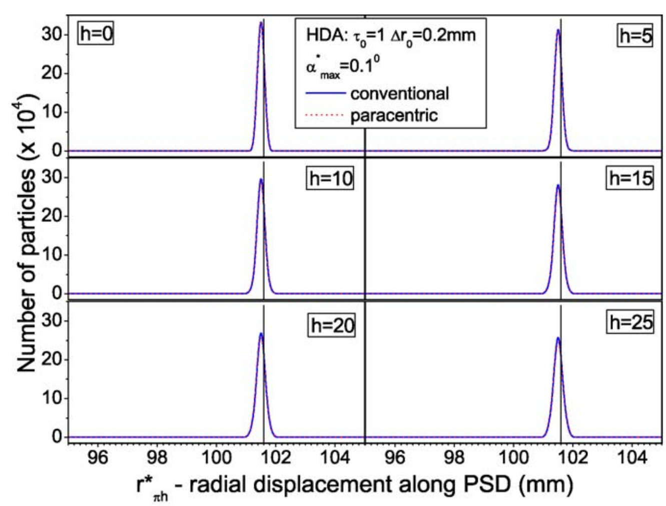

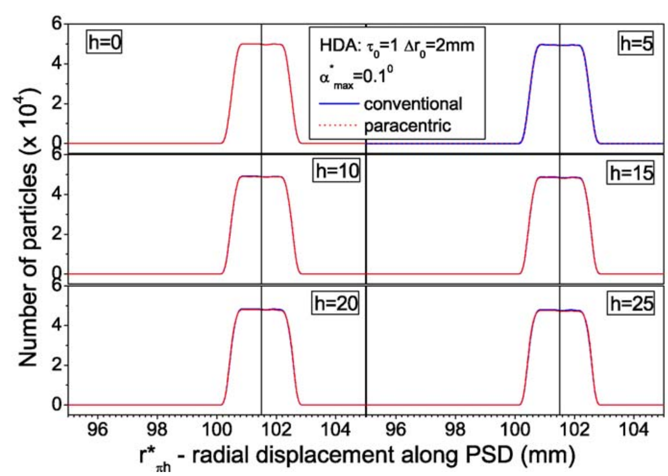

Fig. 8. Line shapes for $h = 0 - 25$ mm for equal sized ($\bar{R} = 101.6$ mm) paracentric ($\xi = 1.2308$ and $\gamma = 1.5$) and conventional ($\xi = \gamma = 1$) HDAs (see Table 1) at $\tau_0 = 1$ with $\Delta r_0 = 0.2$ mm (top) and $\Delta r_0 = 2$ mm (bottom), for $\alpha^*_{\max} = 0.1°$. Lines mark the position of the exit of the central ray with $r_0 = R_0$, $\alpha^* = 0$.

The line shape L_h gives a much more complete picture of the electron-optical characteristics of an HDA. The normalized line shape is also known as the transmission function. L_h can be readily computed either by exact piecewise integration [12,18–20] or Monte Carlo techniques [15,16,21,22] assuming uniform illumination over the entire entry aperture. Here we use the second approach.

$N_{e^-} = 500,000$ monoenergetic electrons were generated with fixed energy τ_0 but random α^* and r_0 values, within the ranges specified by Eqs. (16) and (17), for a specific choice of Δr_0, $\alpha^*_{\rm max}$ and h from the HDA parameters of Table 1. For each specific set of electron parameters, Eq. (12) was used together with Eq. (5) to generate the exit radii $r^*_{\pi h}$ which were then binned using a position resolution of $\Delta r_d = 0.2$ mm to obtain the final distributions. These distributions then represent the response or transmission function of the HDA to a monoenergetic line. The base width of these distributions will correspond closely to the computed value of $\Delta r^*_{\pi h}$ given by Eqs. (26) or (30).

Different line shape calculations were made for $\tau_0 = 0.9, 1.0, 1.1$ representing the 20% energy acceptance window of the HDA, with $\Delta r_0 = 2$ and 0.2 mm representing realistic entry size values, at $\alpha^*_{\rm max} = 0.1^\circ, 1^\circ, 2^\circ, 5^\circ$. For $\alpha^*_{\rm max} < 1^\circ$ and $0 \le h \le 25$ mm, the KS criterion is in general satisfied independent of the value of Δr_0. For larger values of the injection angle and with increasing h, χ_h increases and the KS criterion becomes less valid or eventually even violated. Due to space limitations, the generated characteristic line shapes L_h of equal size (same $\bar{R}$—see Table 1) conventional ($\gamma = \xi = 1$) and paracentric ($\gamma = 1.5$, $\xi = 1.2308$) HDAs are compared here at different values of $h = 0$–25 mm, but only for $\tau_0 = 1$ and $\alpha^*_{\rm max} = 0.1^\circ, 1^\circ, 2^\circ, 5^\circ$. These are shown in Figs. 8–11 for $\Delta r_0 = 0.2$ mm (top), and $\Delta r_0 = 2$ mm (bottom). The value $\alpha^*_{\rm max} = 2^\circ$ is one of the most interesting cases since χ_h varies across 1/2, the KS limit, as h increases from 0–25 mm. For values of $\alpha^*_{\rm max} \le 1^\circ$, L_h does not changes much with h, basically preserving a nice symmetric trapezoidal shape for $\Delta r_0 = 2$ mm or almost triangular shape for $\Delta r_0 = 0.2$ mm with practically no difference between paracentric and conventional HDA. At larger $\alpha^*_{\rm max}$, where the KS criterion is not satisfied, L_h becomes increasing asymmetric with increasing h, peaking on the high energy side of L_h (see Fig. 11). The paracentric HDA is found to have a broader base

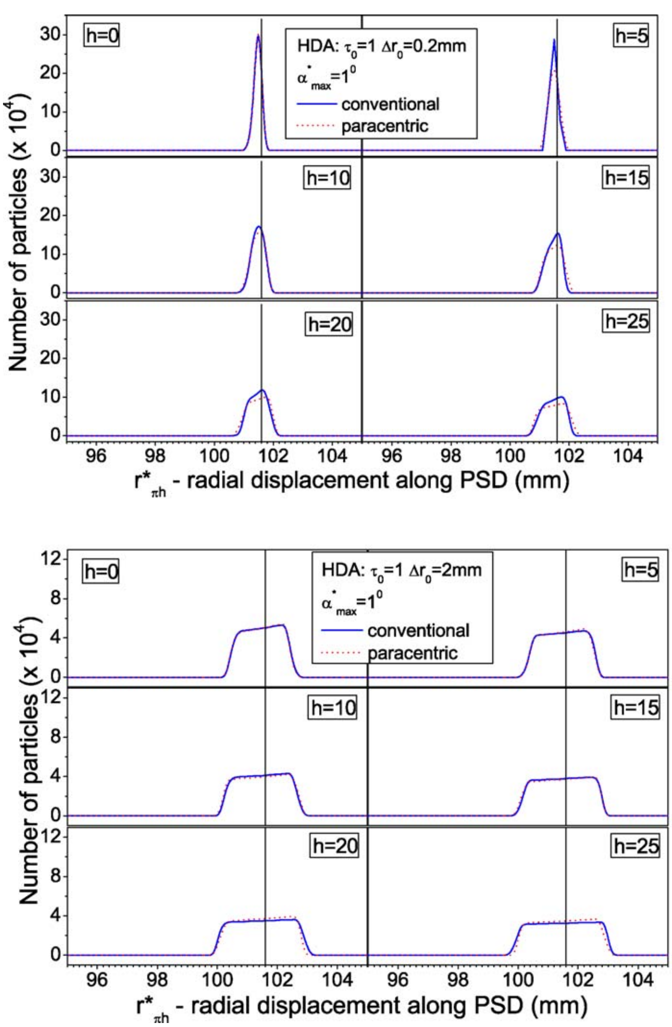

Fig. 9. Same as Fig. 8, but for $\alpha^*_{\rm max} = 1^\circ$.

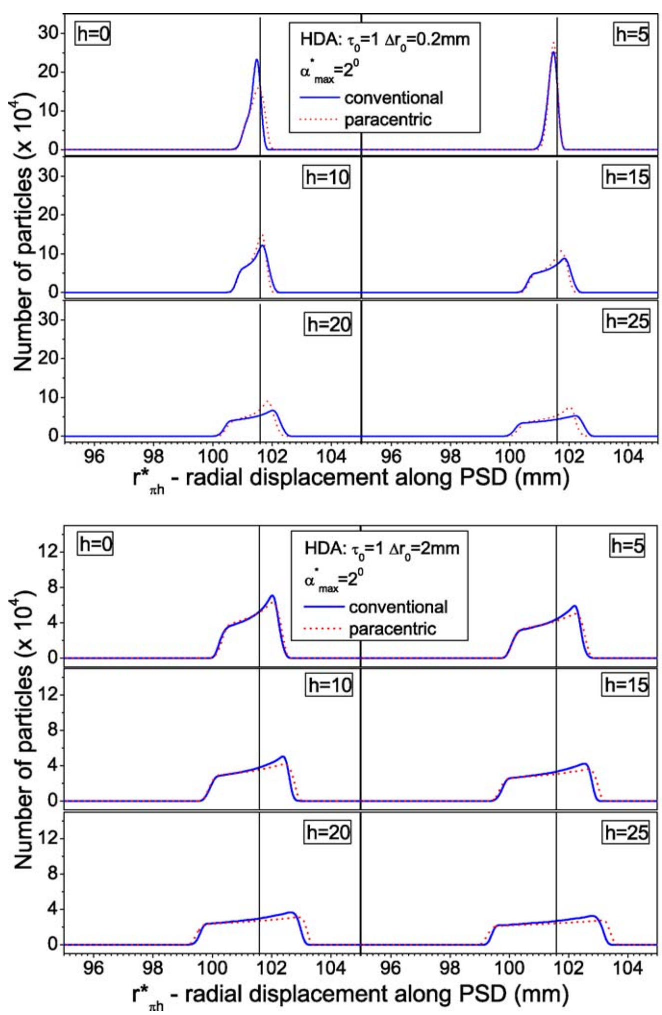

Fig. 10. Same as Fig. 8, but for $\alpha^*_{\rm max} = 2^\circ$. As h varies from 0–25 mm, for $\Delta r_0 = 0.2$ mm the biased paracentric HDA has χ_h (Eq. (41)) vary from 0.460–5.363, while the conventional HDA has χ_h vary from 0.618–4.354. For $\Delta r_0 = 2$ mm the corresponding χ_h variations are 0.08357–0.9753 and 0.1124–0.7919, respectively.

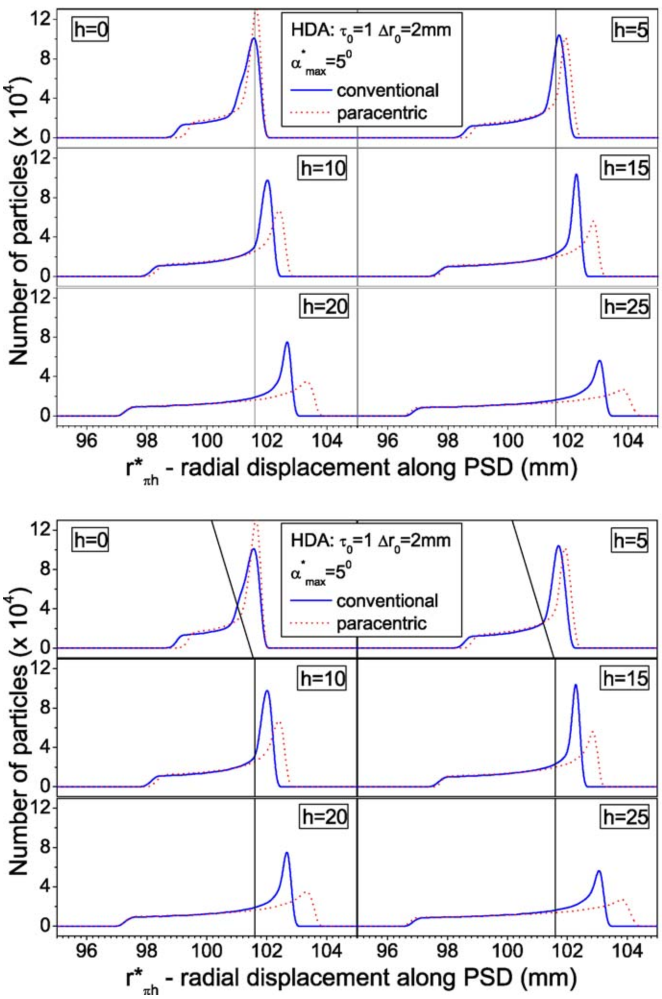

Fig. 11. Same as Fig. 8, but for $\alpha^*_{\max} = 5°$. This angle is probably too extreme for conventional spectroscopy and is only shown for reference.

width than the conventional HDA which, however, for h-values near 0 becomes slightly smaller than for the conventional HDA, as already noted. The line shape and its radial base width do not change much as the energy sweeps across the PSD with τ_0 going from 0.9 to 1.1 (not shown due to space limitations). Thus, the dependence of the base resolution $\mathcal{R}_{Bh}$ on the energy, is strictly a dispersion effect. The dispersion length D increases with energy as already seen in Fig. 2 forcing the corresponding decrease in resolution. This is a well known effect plaguing HDAs with large PSD, the resolution on the low energy side of the PSD being substantially worse than on the high energy side.

3. Summary and conclusions

We have shown that for an ideal HDA, where no fringing fields are considered, the optimal distance to place the PSD for best energy resolution is $h = 0$, the first order focusing plane. Useful analytic formulas of exit radial width $\Delta r^*_{\pi h}$ and base energy resolution $\mathcal{R}_{Bh}$ as a function of the distance from the focal plane h for given maximum injection angle $\alpha^*_{\max}$ and entry aperture diameter Δr_0 are presented. These are further illustrated by line shape calculations at various distances h for specific typical values of $\alpha^*_{\max}$ and Δr_0.

In our presentation we have also made a comparison of equal size *ideal* conventional and paracentric HDAs. Overall, apart from a few marginal improvements of limited utility, the paracentric HDA does not seem to show any significant practical advantages over the conventional HDA. On the contrary, it has a lower dispersion length D and therefore a larger base resolution. However, a smaller D will satisfy the Kuyatt-Simpson criterion (see Eq. (41)) at larger h, thus extending the range of h values over which the quality of the line shape is maintained compared to that of the equal size conventional HDA. The interesting observation that the paracentric HDA exhibits a smaller radial base width $\Delta r^*_{\pi h}$ than the equal size conventional HDA at small h values seems to apply only to angles $\alpha^*_{\max}$ that are too large to be practical in most applications and is therefore probably of only limited interest.

Clearly, fringing field effects must be responsible for the reported improvement [27] in the resolution of the paracentric HDA over that of the conventional HDA and needs to be further investigated. Nevertheless, the analysis of the ideal case (no fringing fields) is necessary as it provides a reference for judging the importance of fringing fields, as deviations from the ideal case. The investigation of the fringing fields of realistic HDAs and their effect on the radial focusing and energy resolution is already under way using specialized electron-optics simulation software (e.g. *SIMION* [36,37]) and will be presented in future publications [32,44].

Acknowledgments

We thankfully acknowledge partial support from the Chemical Sciences, Geosciences and Biosciences Division, Office of Basic Energy Sciences, Office of Science, U S Department of Energy and encouragement from our colleagues at the J.R. Macdonald Laboratory of the Department of Physics at Kansas State University. We also thank Omer Sise of the Dept. of Physics, Afyon Kocatepe University, Turkey for very useful discussions.

References

[1] K. Siegbahn, et al., ESCA-Atomic, Molecular and Solid State Structure Studied by Means of Electron Spectroscopy, vol. 20, Almqvist and Wiksell, Uppsala, 1967.
[2] N. Mårtensson, et al., J. Electron Spectrosc. Relat. Phenom. 70 (1994) 117.
[3] I. Lindgren, J. Electron Spectrosc. Relat. Phenom. 137 (2004) 59.
[4] W. Mehlhorn, J. Electron Spectrosc. Relat. Phenom. 93 (1998) 1.
[5] B. Wannberg, A. Sköllermo, J. Electron Spectrosc. Relat. Phenom. 10 (1977) 45.
[6] J.E. Pollard, D.J. Trevor, Y.T. Lee, D.A. Shirley, Rev. Sci. Instrum. 52 (1981) 1837.
[7] P. Baltzer, B. Wannberg, M.C. Göthe, Rev. Sci. Instrum. 62 (1991) 643.
[8] P.W. Lorraine, B.D. Thoms, W. Ho, Rev. Sci. Instrum. 63 (1992) 1652.
[9] N. Mårtensson, P. Baltzer, P.A. Brühwiler, J.-O. Forsell, A. Nilsson, A. Stenborg, B. Wannberg, J. Electron Spectrosc. Relat. Phenom. 70 (1994) 117.
[10] Y. Ballu, Adv. Electron. Phys., (Suppl. 13B), (1980) 257.
[11] D.W.O. Heddle, J. Phys. E: Sci. Instrum. 4 (1971) 589.
[12] H.D. Polaschegg, Appl. Phys. 9 (1976) 223.
[13] J.C. Helmer, N.H. Weichert, Appl. Phys. Lett. 13 (1968) 266.

[14] F.H. Read, et al., J. Electron Spectrosc. Relat. Phenom. 4 (1974) 293.
[15] D. Roy, J.-D. Carette, Appl. Phys. Lett. 16 (1970) 413.
[16] D. Roy, J.-D. Carette, Can. J. Phys. 49 (1971) 2138.
[17] D. Roy, A. Delage, J.-D. Carette, J. Phys. E: Sci. Instrum. 8 (1975) 109.
[18] M.E. Rudd, Low Energy Electron Spectrometry, in: K.D. Sevier (Ed.), Electrostatic Analysers, Wiley, New York, 1972, p. 17.
[19] F. Hadjarab, J.L. Erskine, J. Electron Spectrosc. Relat. Phenom. 36 (1985) 227.
[20] D. Dubé, D. Roy, Nucl. Instrum. Methods 201 (1982) 291.
[21] Y. Delage, J.-D. Carette, Can. J. Phys. 49 (1971) 2118.
[22] D. Dubé, D. Roy, Y. Ballu, Rev. Sci. Instrum. 52 (1981) 1497.
[23] T. Sagara, L. Boesten, S. Nishida, K. Okada, Rev. Sci. Instrum. 71 (2000) 4201.
[24] V.P. Afanas'ev, S.Y. Yavor, Sov. Phys. Tech. Phys. 20 (1976) 715, (translation of Zh. Tekh. Fiz. 45, 1137–1170, 1975).
[25] E. Granneman, M.V. der Wiel, E.-E. Koch (Eds.), Handbook of Synchrotron Radiation, vol. 1A, North Holland Publishing Company, Amsterdam(1983) p. 367.
[26] S.C. Page, F.H. Read, Nucl. Instrum. Methods Phys. Res. A 363 (1995) 249.
[27] E.P. Benis, T.J.M. Zouros, Nucl. Instrum. Methods Phys. Res. A 440 (2000) 462.
[28] T.J.M. Zouros, E.P. Benis, J. Electron Spectrosc. Relat. Phenom. 125 (2002) 221.
T.J.M. Zouros, E.P. Benis, J. Electron Spectrosc. Relat. Phenom. 142 (2005) 175.
[29] T.J.M. Zouros, E.P. Benis, I. Chatzakis, Nucl. Instrum. Methods Phys. Res. B 235 (2005) 535.
[30] E.P. Benis, et al., Phys. Rev. A 69 (2004) 052718.
[31] T.J.M. Zouros, J. Electron Spectrosc. Relat. Phenom., submitted for publication.
[32] O. Sise, M. Ulu, M. Dogan, and T.J.M. Zouros, J. Electron Spectrosc. Relat. Phenom., submitted for publication.
[33] F. M. Spiegelhalder, O. Sise, T.J.M. Zouros, and D. Manura, Int. J. Mass Spectr., submitted for publication.
[34] V.D. Belov, M.I. Yavor, Nucl. Instrum. Methods Phys. Res. A 470 (2001) 105.
[35] T.J.M. Zouros, E.P. Benis, T.W. Gorczyca, Phys. Rev. A 68 (2003) 010701.
[36] D.A. Dahl, SIMION 3D v6.0, Idaho National Engineering Laboratory, Idaho Falls, 1996.
[37] D.A. Dahl, J.E. Delmore, A.D. Appelhans, Rev. Sci. Instrum. 61 (1990) 607.
[38] C.E. Kuyatt, J.A. Simpson, Rev. Sci. Instrum. 38 (1967) 103.
[39] K.L. Wang, J. Phys. E: Sci. Instrum. 5 (1972) 1193.
[40] A. Poulin, D. Roy, J. Phys. E: Sci. Instrum. 11 (1978) 35.
[41] T.J.M. Zouros, E.P. Benis, Appl. Phys. Lett. 86 (2005) 094105.
[42] T.J.M. Zouros, J. Electron Spectrosc. Relat. Phenom., submitted for publication.
[43] S. Wolfram, The Mathematica Book, 5th ed., Wolfram Media, Chicago, IL, 2003.
[44] T.J.M. Zouros and O. Sise, Appl. Phys. Lett., submitted for publication.